Optics & Laser Technology 174 (2024) 110575

Contents lists available at ScienceDirect

Optics and Laser Technology

journal homepage: www.elsevier.com/locate/optlastec

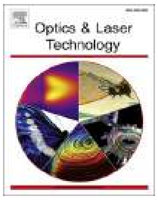

Full length article

Numerical modeling of the temperature distribution and melt flow in dissimilar fiber laser welding of duplex stainless steel 2205 and low alloy steel

Yuelei Zhang [a], Mohammad Hossein Razavi Dehkordi [b,c], Mohammad Javad Kholoud [b], Hamidreza Azimy [b], Z. Li [d,e,*], Mohammad Akbari [b,c,*]

[a] School of Artificial Intelligence, Wuchang University of Technology, Wuhan, Hubei Province 430223, China
[b] Department of Mechanical Engineering, Najafabad Branch, Islamic Azad University, Najafabad, Iran
[c] Aerospace and Energy Conversion Research Center, Najafabad Branch, Islamic Azad University, Najafabad, Iran
[d] Donghai Laboratory, Zhoushan, Zhejiang 316021, China
[e] Faculty of Mechanical Engineering, Opole University of Technology, Opole 45-758, Poland

ARTICLE INFO

Keywords:
Multi-physical simulation
Laser welding
Keyhole
Weld formation

ABSTRACT

The research outlined in this paper pertains to the computational modeling and experimental investigation of laser keyhole welding between duplex stainless steel 2205 and low carbon steel (A516). A crucial aspect of keyhole welding entails predicting the phase transition behavior of the materials involved. The vaporized metal generates a recoil pressure and distorts the interface between the liquid and vapor phases, thus forming a vapor capillary. A multiphysics model employing the finite volume method was proposed to achieve a highly accurate simulation of the temperature and velocity fields. The findings demonstrate that the resulting weld bead relies heavily on the keyhole's structural characteristics. Additionally, analysis of the temperature distribution at a specific temporal and spatial point reveals that duplex stainless steel exhibits elevated temperatures owing to low thermal penetration at a distance of 5 mm from the juncture of the two components compared to A516. The numerical simulation results were in good agreement with experimental results for prediction of temperature filed and melt flow that have impact on weld bead and melt pool geometry. The weld bead width changes according to variation of welding speed and laser power has been in good agreement with the temperature distribution at upper surface of the workpiece extracted from simulation results. The melt pool geometry predicted from the simulation results (melt flow and temperature field) has been in good agreement with the melt pool geometry of the experiment. The temperature distribution from simulation results has a good correlation with the microstructural changes of the melt pool region according to the melting, solidification and temperature gradient at the melt pool region and adjacent HAZ of base metals.

1. Introduction

A modern manufacturing industry is increasingly relying on numerical modeling and simulation, as well as artificial intelligence (AI) modeling [1, 2], optimization techniques [3] and machine learning method [4], to study the manufacturing an industrial process. Also, by using these advanced technologies (numerical modeling, simulation of the process, artificial intelligence, optimization, and machine learning), a precise understanding of the temperature distribution and melt flow in dissimilar fiber laser welding can be achieved. Such technologies not only enable more accurate prediction of the welding process but also enable the control and optimization of welding parameters to improve welding quality [5–7]. Due to the increasing need for combining two materials in numerous industries, dissimilar laser welding between A516 carbon steel and duplex stainless steel has attracted a lot of interest lately [8]. While duplex stainless steel offers good mechanical and corrosion resistance, A516 carbon steel is frequently utilized in structural components. These materials combined offer a special set of qualities that can be useful in a variety of applications. Dissimilar laser welding is the method of fusing two distinct materials together by heating them with a laser beam. In comparison to conventional welding techniques, laser welding has a number of benefits, such as accurate heat input control, little distortion, and a small heat-affected zone. Due to

---

* Corresponding authors.
E-mail addresses: z.li@po.edu.pl (Z. Li), m.akbari.g80@gmail.com (M. Akbari).

https://doi.org/10.1016/j.optlastec.2024.110575
Received 15 September 2023; Received in revised form 5 December 2023; Accepted 8 January 2024

Nomenclature

h	heat transfer coefficient, W/m^2K
$\bar{u}$	mean velocity, m/s
P	Pressure, N/m^2
X.Y.Z	Cartesian coordinates
C	specific heat capacity, J/kgK
T	Temperature,K
t	time,s
H	enthalpy, J
H_v	evaporation latent heat,J
k	thermal conductivity, W/mK
u, v, w	velocities components in X,Y and Z directions, m/s
q	heat flux, W/m^2
F,a,b,c,d	distribution coefficients
K_0	constant of the mushy zone
F	VOF function
S_V	energy equation source term
P_r	recoil pressure,pa
f	Liquid fraction
W	evaporation rate, g/s
M	molar mass, g/mol
N	Avogadro's number
A	pressure coefficient
B	evaporation constant
k_b	Boltzmann constant

Greek symbols

ρ	density, kg/m^3
μ	dynamic viscosity Pa s
ϑ	kinematics viscosity, m^2/s
β	thermal expansion coefficient,1/K

these advantages, laser welding is a desirable choice for combining materials of varied properties, especially in situations where the melting points and thermal characteristics of the materials are significantly different. Due to their distinct metallurgical properties and chemical compositions, welding A516 carbon steel and duplex stainless steel creates a number of difficulties. The development of brittle intermetallic phases, changes in thermal conductivity, and different solidification behaviors are some of these difficulties. It is essential to create suitable welding settings and improve the process conditions in order to get past these obstacles and produce a strong weld [9,10]. Understanding the intricate physics of dissimilar laser welding between duplex stainless steel and A516 carbon steel depends critically on modeling. Researchers and engineers can mimic the heat transfer, fluid movement, and phase transitions that occur during the welding process by creating precise models. These models enable the prediction of weld quality and performance by offering insights into the evolution of temperature, microstructure, and residual stresses [11]. For laser processing to produce the appropriate weld and cut quality and mechanical qualities, optimization approaches are crucial [12]. With these methods, welding parameters such as laser power, welding speed, focal position, and shielding gas composition are systematically explored. The goal is to identify the ideal set of variables that minimizes flaws, increases joint strength, and produces dependable welds. Artificial neural networks and genetic algorithms are two examples of sophisticated optimization algorithms that are frequently used to effectively search the parameter space and determine the ideal welding and cutting surface conditions [13]. These algorithms cater to process limits and limitations while taking into account several objectives, such as decreasing intermetallic phase development and increasing joint strength. So far, studies have been done on the dissimilar laser welding of different alloys. In an experimental study, Karimi et al. [8] investigated the mechanical properties and effective parameters in the dissimilar laser welding process. Their outcomes demonstrated that the most effective parameter is laser power and the fusion zones on both sides of the weld line are composed of two different phases. In a numerical-experimental study, Jung et al. [14] investigated the effect of laser welding angle to prevent laser head interference. The results demonstrated that the optimal value of the angle is 20 degrees and the results are in good agreement. Sun et al. [15] investigated the temperature distribution behavior and heat transfer mechanism in the dissimilar laser welding process of austenitic stainless steel and martensitic stainless steel. The outcomes showed that Marangoni stress and buoyancy force are the most important factors affecting welding quality. Khdair et al. [16] investigated the effects of laser welding parameters on the shape of the weld bead, the microstructure of the molten pool, the temperature field around the molten pool, and the dimensions of the molten pool. The results showed that changing the speed of laser welding improves the quality of the weld bead and changes the microstructure. Also, this parameter affects the temperature of the pool and these changes ultimately lead to determining the dimensions of the molten pool. Nguyen et al. [17] presented a non-linear model using the Hammerstein–Wiener method for inhomogeneous laser welding of S.S 304 and Acrylonitrile Butadiene Styrene (ABS). The results showed that this model has a simpler structure and good accuracy while requiring less calculations. In another study [18], Nguyen et al. investigated temperature distribution and mechanical properties for dissimilar laser welding of austenitic stainless steel and copper. By examining the results, it was found that with increasing laser power, the hardness of the fusion zone decreases, while the dimension of the molten pool increases. Baghdadchi et al. [19] investigated the mechanical properties of duplex stainless steel in the laser welding process in the presence of shielding gas and laser reheating. By examining the results, it was found that the combination of welding with pure nitrogen as shielding gas and a laser reheat scan can significantly improve the formation of austenite and reduce the formation of nitrides in duplex stainless steel (DSS) laser welds. Using a numerical method, Mosavi et al. [20] evaluated the mechanical properties and temperature distribution during laser welding of AISI 304 and AISI 420. By examining the results, it was found that the welding speed has the greatest effect on the tensile strength of the connection. Landowski et al. [21] evaluated the quality of welded joints in the laser welding process of 316L Austenitic and 2304 duplex stainless steels. Examining the results, it was found that the welded joints meet the level B acceptance criteria according to the EN ISO 13919–1 standard. Saravanan et al. [22] evaluated the quality of duplex stainless steel welded joints made by Nd:YAG laser. By examining the results, it was found that the welding speed has an effect on the amount of ferrite or austenite present due to temperature changes. Lai et al. [23] evaluated the effect of shielding gas on the mechanical properties of 2205 duplex stainless steel during laser welding. The results showed that the use of nitrogen shielding gas increases the weld corrosion resistance. Chen et al. [24] investigated the weld quality of A516 Gr.70 during laser welding. The results demonstrated that by using laser welding compared to electron beam welding, a weld with proper penetration and higher hardness can be achieved.

It can be concluded, dissimilar laser welding between Duplex stainless steel and A516 carbon steel offers excellent potential for joining materials with a variety of purposes. By utilizing modeling, simulating and optimization approaches, scientists and engineers may get around the challenges of joining different materials and making high-quality welds. These advancements in dissimilar laser welding contribute to the development of fresh ideas in a variety of industries, including biomedical use, automotive design, and structural and civil engineering. The novelty of this research is the use of a new numerical model using a hybrid heat source to simulate the complex dynamics associated with keyhole characteristics. Also, an in-depth analysis of the keyhole phenomenon will be presented, and its results will be discussed. In addition, the obtained results will be compared with experimental data.

2. Experimental procedure

Dissimilar laser welding experiments was performed on a 2 axis interpolation CNC table equipped with NC-Studio software. A continuous wave (CW) fiber laser with BW210 laser welding head was used for welding process. A copper side below nozzle at inclination angle of 30° related to the welding nozzle axis was used to apply argon gas with 1.6 lit/min flow rate for protecting melt pool region. Two k-type thermocouples with 1 mm diameter was utilized to measure the temperature variation during laser welding process. A groove with diameter of 1.1 mm and depth of 0.85 mm was engraved on parts to locate the thermocouples at defined coordinate of 2 mm from the center of the melt pool. The chemical composition of utilized materials for laser welding has been shown in Table.1. The USB4718 portable thermocouple module including 8 channels of thermocouple inputs with 16-bit resolution and accuracy of 0.1 % of input range was utilized to convert the analog signals of thermocouples to data for LABVIEW software to collect and save temperature data. The Olympus microscope model BX51 was utilized to provide images from weld cross section. For metallography analysis, the welded samples were hot mounted and grounded from 150 to 1200 grit size on sic paper and finally polished. The Olympus stereoscopes model SZX18 was utilized to provide the images from weld bead surface. An image of the lase welding experimental setup is observed in Fig. 1.

Fig. 1. Actual view of the laser welding experiments.

3. Numerical simulation

The correlation between the temperature gradient and the dynamic properties of liquid metal and plasma within the keyhole has a direct impact on the weld's quality, dimensional characteristics, and mechanical attributes of the fused metal. Consequently, the anticipation of influential factors pertaining to heat transfer, fluid dynamics, and the formation of metal vapor patterns within the keyhole is crucial for enhancing welding quality and minimizing the need for extensive testing. To numerically simulate fiber laser welding, a transient computational model utilizing the finite volume method (FVM) was employed. In this investigation, an accurate assessment of material behavior during the welding process involving dissimilar duplex and low carbon steel metals was achieved by simulating solid, liquid, and vaporized metal phases. Fig. 2 portrays a visual representation of the relevant workpieces involved. To facilitate a comprehensive analysis of temperature distribution variations resulting from alterations in laser welding parameters, the modifications were meticulously observed at a prescribed proximity of 20 mm from the initial section of the workpiece.

3.1. Modeling of laser welding process

In laser keyhole welding, the division of energy absorbed from the laser beam into distinct components is a fundamental characteristic. A portion of this energy is absorbed at the surface, while another portion is absorbed at the keyhole's wall. To accurately represent the absorbed energy on the keyhole walls' surface, the cylinder heat source was deliberately employed, whereas the double ellipsoidal heat source was selected for energy absorption on the keyhole's surface. Fig. 2 provides a schematic representation of the thermal model, while Eqs. (1) to (3) present the desired thermal model [10,25,26].

$$q_v(x,y,z) = \frac{6f\eta p}{\pi r_v^2 d} e^{\left(-3\frac{\left(x^2+y^2\right)}{r_v^2}\right)\left(\frac{mz+r_v}{md+2r_v}\right)} \tag{1}$$

$$q_f(x,y,z) = \frac{6\sqrt{3}ff_f\eta p}{a_f bc\pi\sqrt{\pi}} e^{-3\left(\frac{x^2}{a_f^2}+\frac{y^2}{b^2}+\frac{z^2}{c^2}\right)} \tag{2}$$

$$q_r(x,y,z) = \frac{6\sqrt{3}ff_r\eta p}{a_r bc\pi\sqrt{\pi}} e^{-3\left(\frac{x^2}{a_r^2}+\frac{y^2}{b^2}+\frac{z^2}{c^2}\right)} \tag{3}$$

The energy distribution of the double ellipsoidal heat source in the front

Table 1
Chemical composition of duplex 2205 and A516 alloy [8].

Composition		C%	S%	Cr%	Mn%	P%	Si%	Ni%	MO	Fe
Weight	Duplex 2205	0.04		23	2.1		1	6.5	3.5	Bal.
	A516	0.2	0.03	0.3	1.7	0.03	0.6	0.3	0.08	Bal.

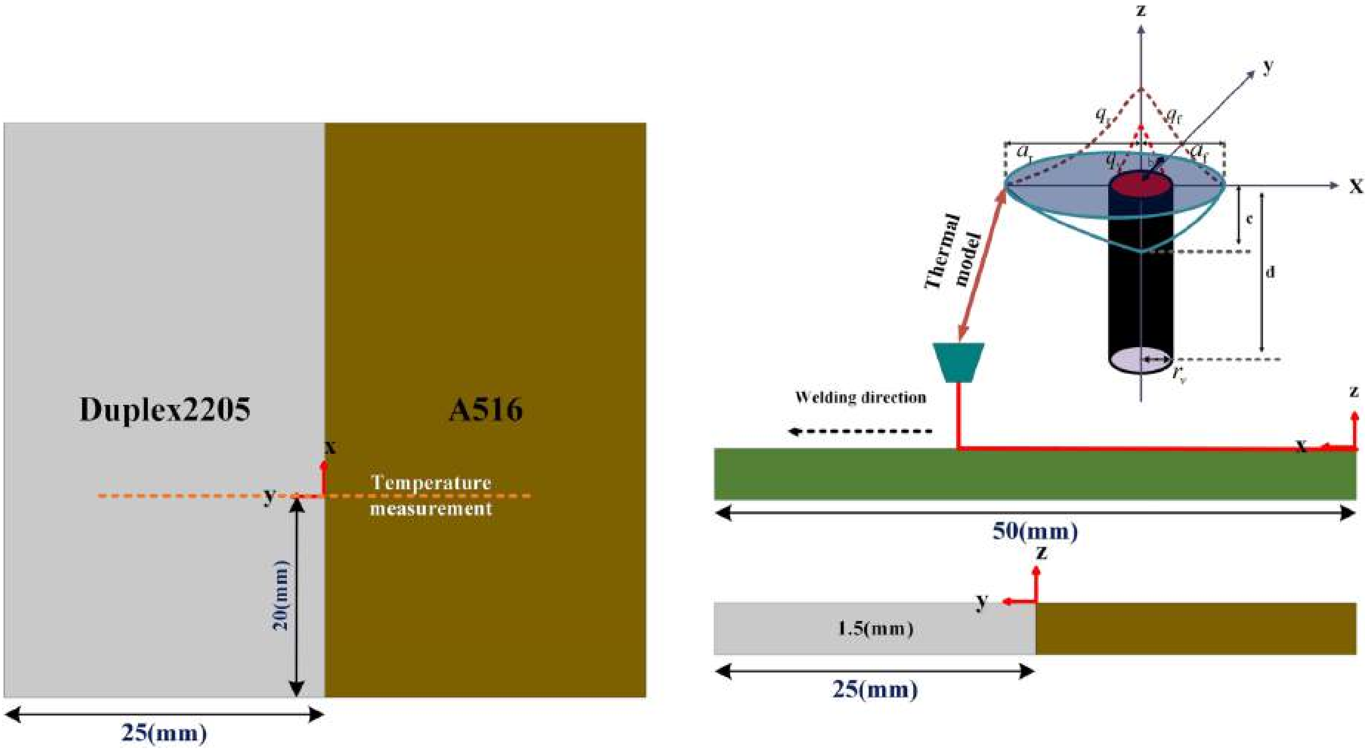

Fig. 2. A view of the workpiece and thermal model from a) top view coordinate, b) cross section of workpiece and thermal model properties.

and rear of laser beam is represented by q_f and q_r, respectively, while q_v denotes the energy distribution within the cylindrical heat source. The distribution factors of the heat deposited in the front and rear quadrants of the ellipsoid are f_r and f_r. For the cylindrical heat source and the double ellipsoid heat source, the energy distribution coefficients are f. The parameters a_f, a_r, b, and c determine the ellipsoid's size and form that are specified in Table 2. h is equal to the thickness of the sheets. The damping coefficient is m, and radius of heat source is determined according to the spot radius (0.5 mm). P is the laser welding power, and η is the absorption coefficient which was determined based on the emissivity for each workpiece [29]. Fig. 3 shows the comparison of the shape of the molten pool resulting from numerical simulation and experimental work for power = 400 W and speed = 4 mm/s. As observed, the presented thermal model has been able to predict the dimensions of the molten pool well.

3.2. Governing equations

The unified computational domain effectively addresses the three distinct states of matter, namely solid, liquid, and gas. The governing equations, pertaining to mass, momentum, and energy, are denoted as presented [26,37].

Continuity equation:

$$\nabla.\left(\rho\vec{U}\right) = 0 \tag{4}$$

Momentum equation:

The intermediate region characterized by a transitional state between solid and liquid phases is considered as a porous medium. The source term incorporates the isotropic permeability obtained from the Carman-Kozeny equation, thereby introducing an additional parameter [38].

$$\frac{\partial\left(\rho\vec{U}\right)}{\partial t} + \nabla.\left(\rho\vec{U}\vec{U}\right) = -\nabla p + \nabla.\left(\mu\nabla\vec{U}\right) + \rho\vec{g} - \frac{\mu}{K_0\frac{f^3+\tau}{(1-f)^2}}\vec{U} \tag{5}$$

Energy equation:

$$\frac{\partial(\rho H)}{\partial t} + \nabla.\left(\rho\vec{U}H\right) = \nabla.(k\nabla T) + S_V \tag{6}$$

The volume of fluid (VOF) strategy was employed to carry out the numerical simulation. A novel governing factor, denoted as F, is submitted to quantify the proportion of molten material. The value of F for each computational cell undergoes temporal variations and can be determined based on the inflow and outflow volumes within that cell. When $0< F <1$, the cell encompasses the interface between the liquid and vapor phases. Consequently, the equation characterizing the volume of molten material in the flow can be expressed as follows [37]:

$$\frac{\partial F}{\partial t} + \nabla.\vec{U}F = 0 \tag{7}$$

3.3. Boundary conditions and computational domain

The incorporation of recoil pressure P_r and surface tension P_σ into the equation of motion conservation as a source term is primarily intended to ensure the dynamic equilibrium of the keyhole's surface. These parameters play a crucial role in sustaining the stability of the keyhole throughout the calculation process [39].

$$P = P_\sigma + P_r \tag{8}$$

$$P_r = ABT_s^{-0.5}e^{\left(\frac{-m_a H_v}{N_a k_b T_s}\right)} \tag{9}$$

Table 2
Parameters of the heat source model [15,27–36].

Parameters	f_f	f_r	r_v	a_r/h	a_f/h	b/h	c/h	d/h
Values	0.25	0.75	Spot radius	0.15	0.25	0.275	0.15	1

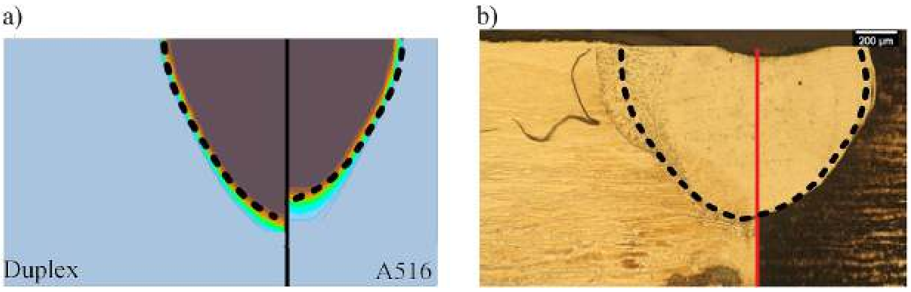

Fig. 3. Weld profile comparison a) simulation and b) experiment.

Eqs. (10) and (11) define the characterization of shear stress exerted on the surface of the workpiece due to the gradient in surface tension and the generation of Marangoni flow within the liquefied pool [25].

$$\mu\frac{\partial u}{\partial z} = -\frac{\partial \gamma}{\partial T}\frac{\partial T}{\partial x} \tag{10}$$

$$\mu\frac{\partial v}{\partial z} = -\frac{\partial \gamma}{\partial T}\frac{\partial T}{\partial y} \tag{11}$$

The thermal boundary conditions pertaining to laser absorption, heat convection, radiation, and evaporation can be formulated to describe the keyhole's free surface, as follows [34,40]:

$$k\frac{\partial T}{\partial \vec{n}} = -\varepsilon\sigma\left(T^4 - T_\infty^4\right) - h(T - T_\infty) - WH_v \tag{12}$$

The pressure outlet serves as the prescribed boundary condition for the upper surface within the computational domain. The remaining surface boundaries, comprising the lower and lateral surfaces, are established as wall conditions, wherein heat loss due to radiation and convection is accounted for in the thermal boundary of the walls.

$$k\frac{\partial T}{\partial \vec{n}} = -\varepsilon\sigma\left(T^4 - T_\infty^4\right) - h(T - T_\infty) \tag{13}$$

A computational domain model was defined, as illustrated in Fig. 4. Specifically, the gas phase is delineated by designating the upper layer of the mesh model with a thickness of 2 mm. It is imperative to acknowledge that diminishing the dimensions of the cells and augmenting their abundance engenders a protracted procedural course. Conversely, amplifying the magnitude of grid constituents diminishes the precision of computations and the faculty to discern phenomena. Consequently, assessing grid autonomy to acquire the optimal value for the number of constituents becomes indispensable. In this investigation, the number of constituents after the mesh-independency was derived to be approximately 750000.

3.4. *Thermophysical properties*

Table 3 illustrates the thermophysical properties of duplex stainless steel and low carbon steel A516 alloy at a temperature of 298 K. Consequently, the thermophysical characteristics related to temperature variation were determined due to the modifications occurring at high temperatures during the process of laser welding. Fig. 5 shows the values of density, thermal conductivity and specific heat capacity in terms of temperature for duplex 2205 and A516 alloy.

Table 3
Thermophysical characteristics of duplex 2205 and A516 alloy [41–46].

Nomenclature	Symbol	Material	Value	Unit
Solid phase density	ρ_s	Duplex 2205	7860	kg/m^3
		A516	7800	
Solidus temperature	T_s	Duplex 2205	1658	K
		A516	1683	
Liquidus temperature	T_l	Duplex 2205	1773	K
		A516	1733	
Temperature in the surrounding	T_∞		298	K
Thermal conductivity	k	Duplex 2205	19	W/m.K
		A516	52	
Specific heat	c	Duplex 2205	0. 418	J/g.K
		A516	0. 470	
Melting latent heat	L_m	Duplex 2205	5×10^5	J/kg
		A516	2.7×10^5	
Stefan-Boltzmann constant	σ		5.67×10^{-8}	W/m^2.K^4

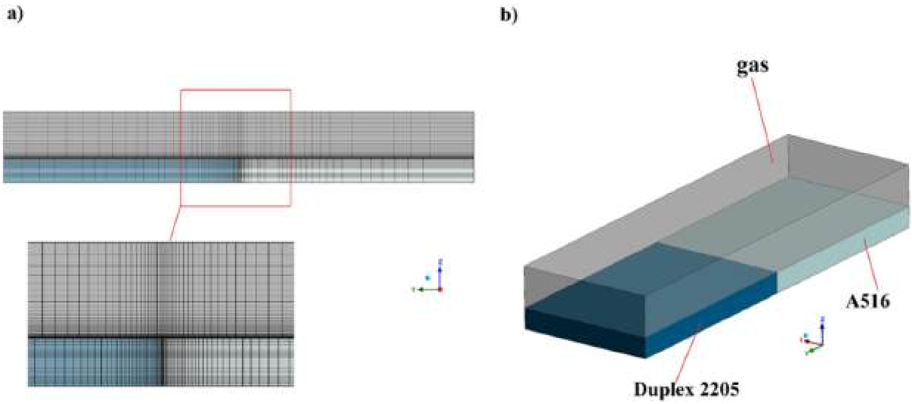

Fig. 4. A view of the mesh model.

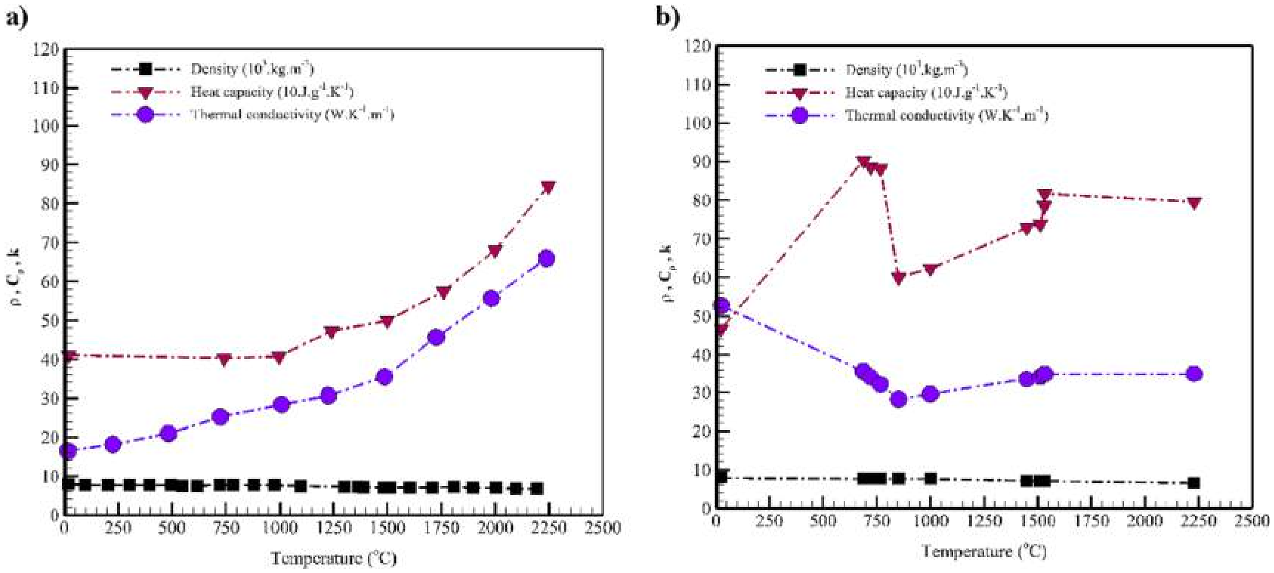

Fig. 5. Thermophysical properties of a) duplex 2205 and b) A516 alloy [41–46].

4. Results and discussions

4.1. Thermal assessment

Temperature dispersion evaluation is a paramount factor that impacts the welding quality and the extent of the heat-affected zone in keyhole welding. Consequently, this section delves into scrutinizing the influence of average alterations in energy levels and welding speed on the field of temperatures during the welding process of two disparate metals.

4.1.1. Power effect

Fig. 6 displays the temperature variation at distinct lateral distances on the component's surface under varying input power conditions. The observations were documented for a welding velocity of 5 mm/s, precisely at a distance of 20 mm from the initial section of the components (illustrated in Fig. 2) and at a temporal instance of 4 s. The data presented in Fig. 6 illustrates that the low carbon steel component has undergone elevated temperatures at varying distances in contrast to duplex stainless steel. This discrepancy arises from thermal conductivity dominated by the 516 piece. Nevertheless, upon meticulous

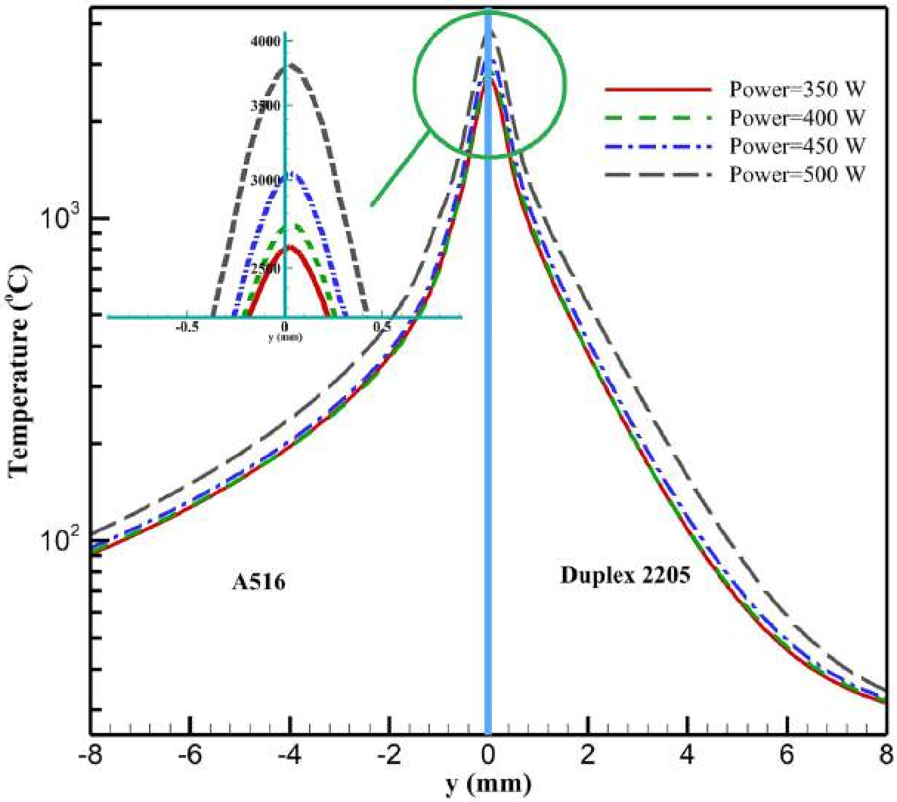

Fig. 6. Temperature on the surface of parts in the transverse direction at different powers.

examination of the temperature variations close to the junction between the two components, no noteworthy disparity is discernible, and the temperature gradient exhibits near-equivalence along the y-axis orientation. Moreover, it is evident that a surge in laser power by 150 W results in a substantial elevation of approximately 1200 °C in the temperature at the point of convergence between the two components.

Fig. 7 illustrates the temporal variations in temperature for average input powers ranging from 350 to 500 W at a speed of 5 mm/s and positioned at a distance of 20 mm from x = 0. The depicted graph reveals that the temperature increment does not exhibit a linear relationship with the growth in average power. Notably, the temperature at its peak experiences a surge up to 3800 °C upon the escalation of power from 450 to 500 W. This figure shows how increasing the power to 450 W causes the maximum temperature to occur earlier. This is because latent heat limits the temperature rise. However, the keyhole becomes unstable with an increase of 50 W of power, and this has caused a change in the temperature history pattern. This outcome result from the disparate thermophysical characteristics exhibited by the respective components.

Figs. 8 and 9 present the thermal distribution on the surface and cross-sectional area of the interface between two components, respectively. Based on Fig. 7, it is evident that alterations in energy density yield negligible impacts on the temperature dispersion while augmenting laser power results in an expanded range of temperatures. In general, a salient characteristic of laser welding lies in its propensity for confining the thermally influenced zone compared to alternative techniques. The manifestation of this attribute is visibly discernible in Fig. 8, wherein the temperature distribution across the surface of the components is depicted. Fig. 9 illustrates the temperature distribution occurring at the interface between two entities, observed under varying power densities across four distinct scenarios. The presented graphical representation unmistakably portrays that alterations in laser power exclusively induce temperature field within the laser beam's immediate vicinity, which diminish substantially as the distance from the source increases.

4.1.2. *Speed welding effect*

Fig. 10 shows the temperature changes at different transverse distances along the part surface at x = 20 mm (Fig. 2) while different laser welding speeds were applied. The graphical representation can infer that the duplex stainless steel component had lower temperature levels than the low carbon steel at significant distances from the joint. However, near the interface between the two components, the duplex part shows the highest temperature, which is attributed to the low thermal conductivity of duplex stainless steel. Fig. 11 depicts the temporal evolution of temperature observed at a 5 mm offset from the juncture between two components during various welding speeds. Upon examining the temporal patterns of temperature variations for both specimens under different velocities, it is evident that the profiles are nearly identical. The duplex component consistently exhibits higher temperatures across all velocities, which is due to its low thermal conductivity. Temperature measurements were recorded at a specific location denoted as x = 20 mm.

Fig. 12 shows the effect of laser welding speed changes in the average power of 400 W applied on the part surface. It can be seen that by increasing the welding speed from 3 to 6 mm/s, there is a significant decrease in heat penetration to the adjacent areas. This phenomenon is attributed to the decrease in the absorption time of the laser beam energy, and as a result, it leads to a decrease in temperature. It can also be seen carefully from the figure that the increase in speed has led to the ellipse of the constant temperature lines.

4.2. *Keyhole pattern*

Keyhole laser welding involves the utilization of exceedingly high beam intensities for material processing. In contrast to heat conduction welding, this technique gives rise to the formation of metal vapor alongside the metal melt. Consequently, the vapor displaces a portion of the melt, forming a vapor column known as the "keyhole." By directly imparting energy into the material, this method maximizes weld depth

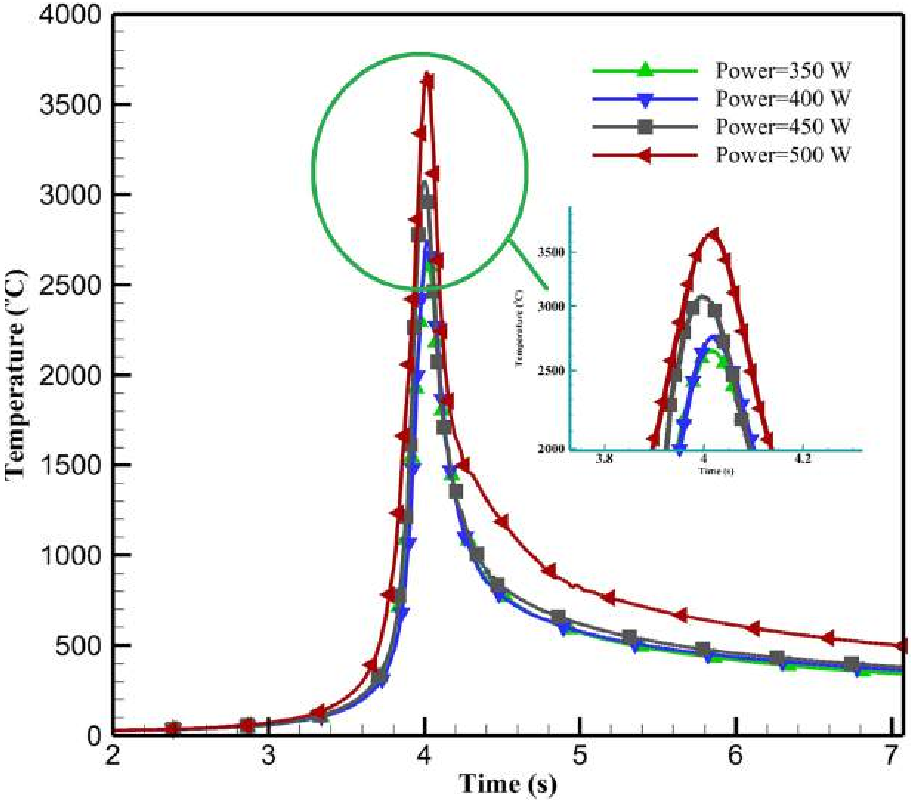

Fig. 7. Temperature history in different laser energy at a welding speed of 5 mm/s and different powers.

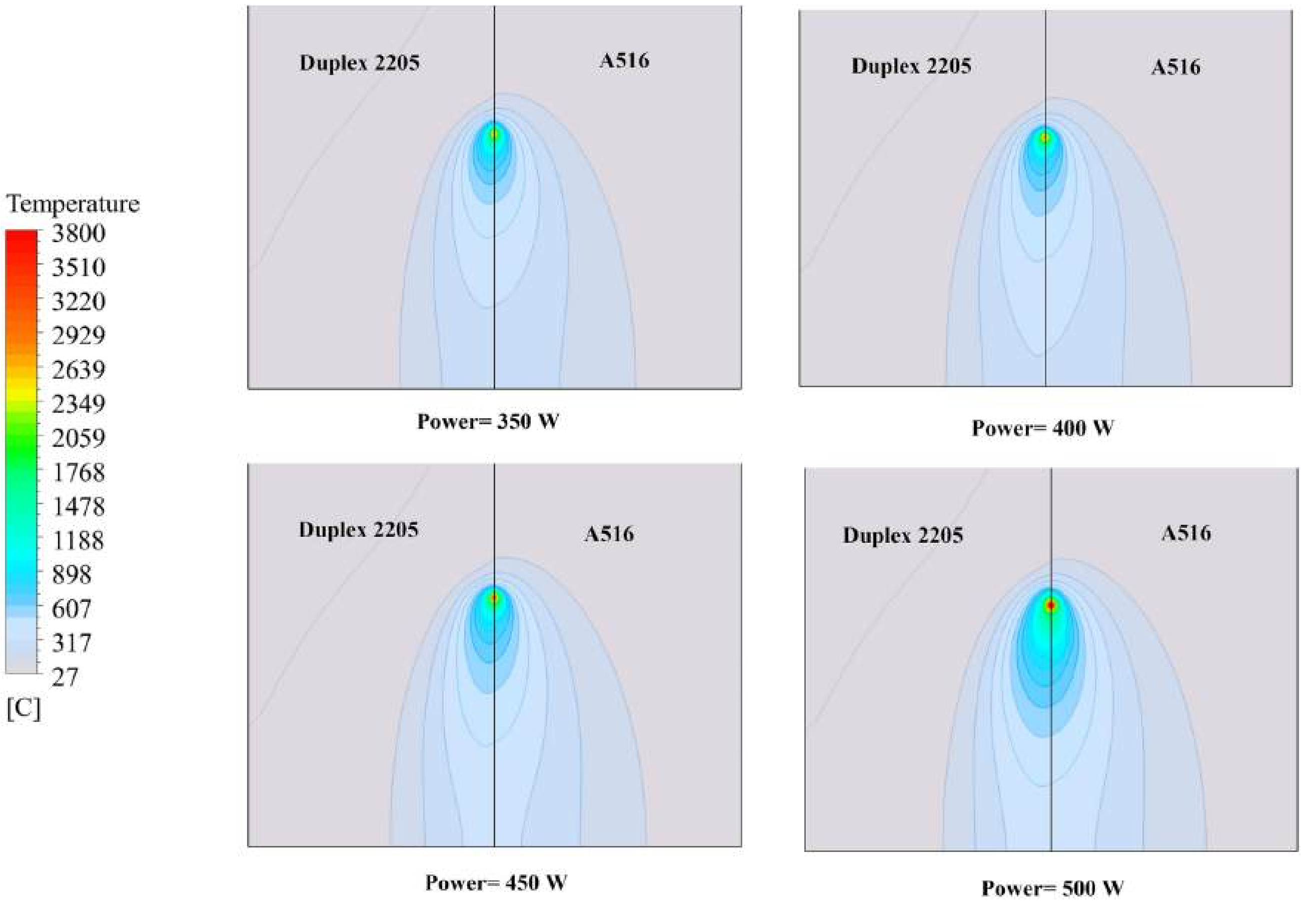

Fig. 8. Temperature field on the surface of workpieces at different powers.

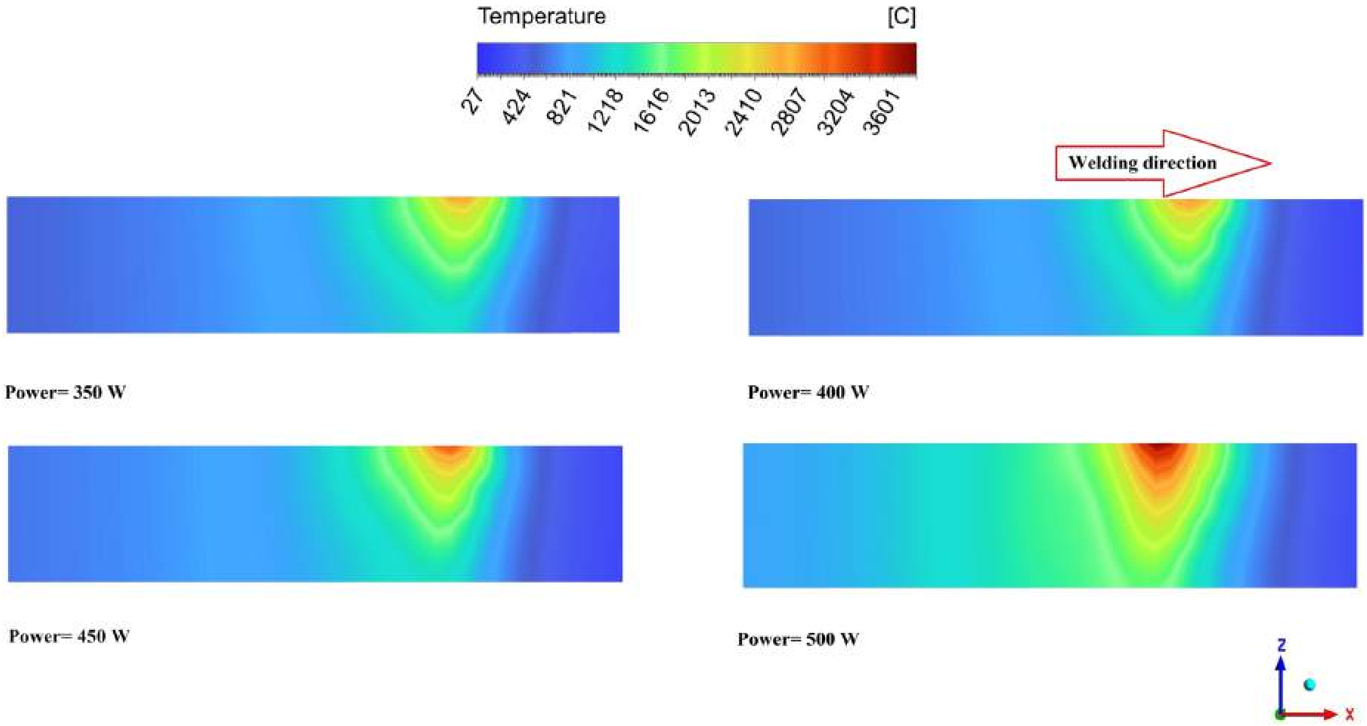

Fig. 9. Temperature distribution at the interface of two workpieces at different powers.

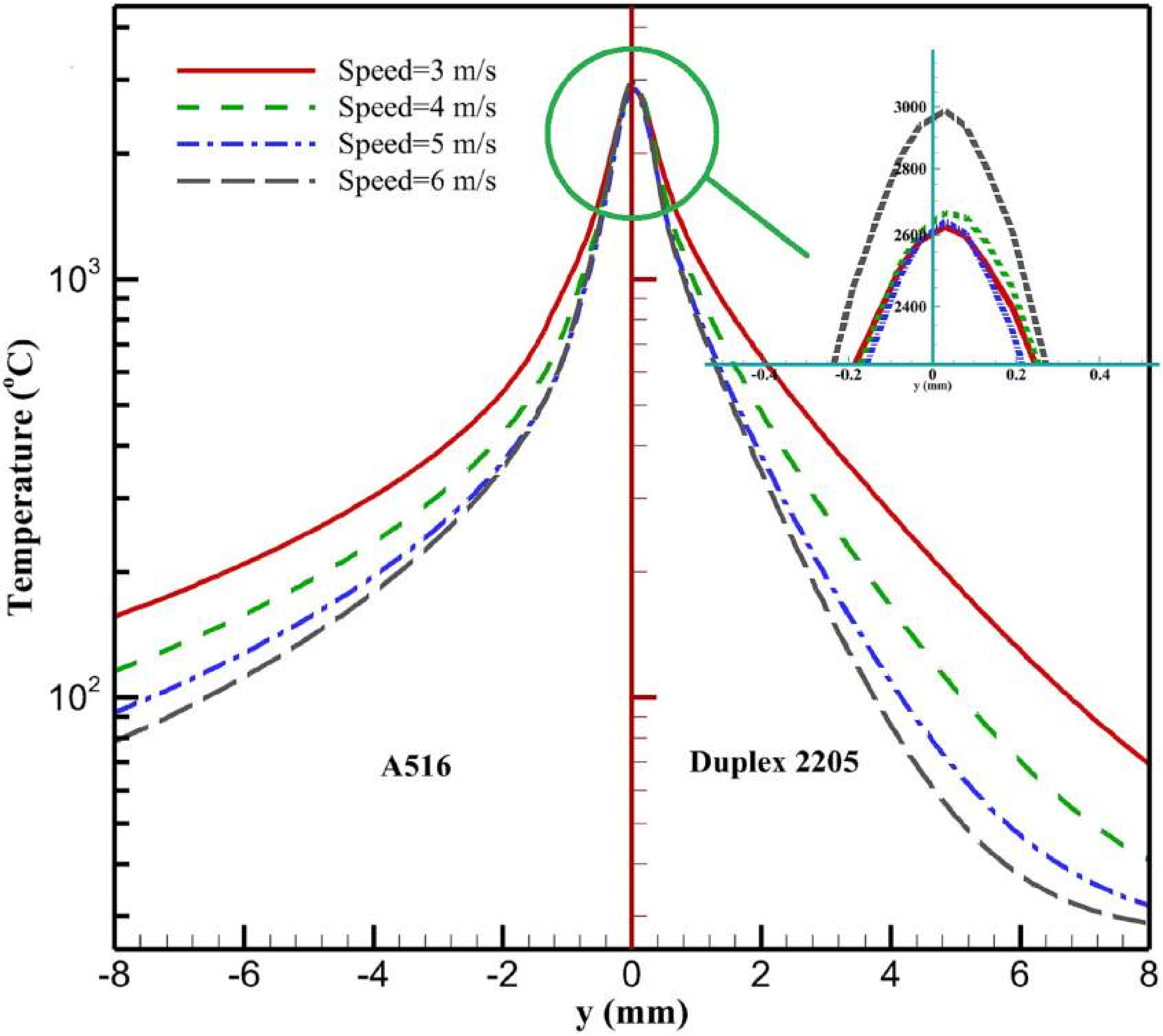

Fig. 10. Temperature difference on the surface of parts in the transverse direction at different welding speeds.

while minimizing the transfer of heat to the material. As a result, both the heat affected zone and part distortion are reduced. Under stable conditions and optimized welding parameters, the vapor pressure within the keyhole effectively prevents the liquefied material from collapsing permanently, which would terminate the welding process. However, intermittent collapses of the keyhole on a local scale and within a short timeframe may still occur, even during an optimized weld. Hence, the present investigation endeavors to anticipate the occurrence of the keyhole at various temporal instances by applying computational techniques. Utilizing this numerical simulation holds the potential to unravel vague occurrences within the during of laser welding.

The keyhole formation within the shared plane of duplex stainless steel and low carbon steel is visually depicted in Fig. 13, where a power setting of 450 W and a welding speed of 5 mm/s are employed. The velocities of the molten material beneath the keyhole exhibit a notable increase due to the restricted interstice between the lower part of the keyhole and the solid substrate, as well as the flow velocity of the protrusions. The formation of this restricted interstice occurs when the molten material at the lower part of the keyhole is propelled by the recoil pressure resulting from the narrow gap between the lower part of the keyhole and the solid substrate, thereby diminishing the available space for flow and leading to a relatively higher velocity. Likewise, the heightened velocity of the fluid in the vicinity of the protrusions arises from the more excellent absorption of laser energy in this area owing to its irregular shape. The molten material flow behind the liquefied pool undergoes retrograde motion influenced by the recoil pressure, thereby generating a vortex in this region. Based on the figure, the observation reveals that within a time of 36 ms, a ripple occurs on the surface as a consequence of the recoil pressure and solidification of the liquefied material on the workpiece's surface. As time progresses, owing to the progressive assimilation of additional energy, the aperture undergoes complete expansion, establishing a metallic vapor column. By considering the principle of buoyancy, it becomes evident that the vapor particles tend to exit from the keyhole.

Fig. 14 illustrates the interaction among the solid region, the molten pool, and the metal vapor under the conditions of 500 W power and 5 mm/s welding speed. Comparing it with Fig. 14, it is evident that the keyhole was formed earlier due to heightened energy absorption. Detailed examination of Fig. 14c reveals that the extreme temperature gradient drives the vapor movement within the keyhole near the wall. Furthermore, the keyhole's front wall exhibits the highest velocity owing to enhanced thermal penetration. Moreover, Fig. 14d demonstrates the creation of an imbalanced hole on the piece's surface, which arises from the distinct thermophysical properties of the two components. Fig. 14d (top view) indicates that the duplex piece creates a larger cavity surface than low carbon steel by performing as a heat source.

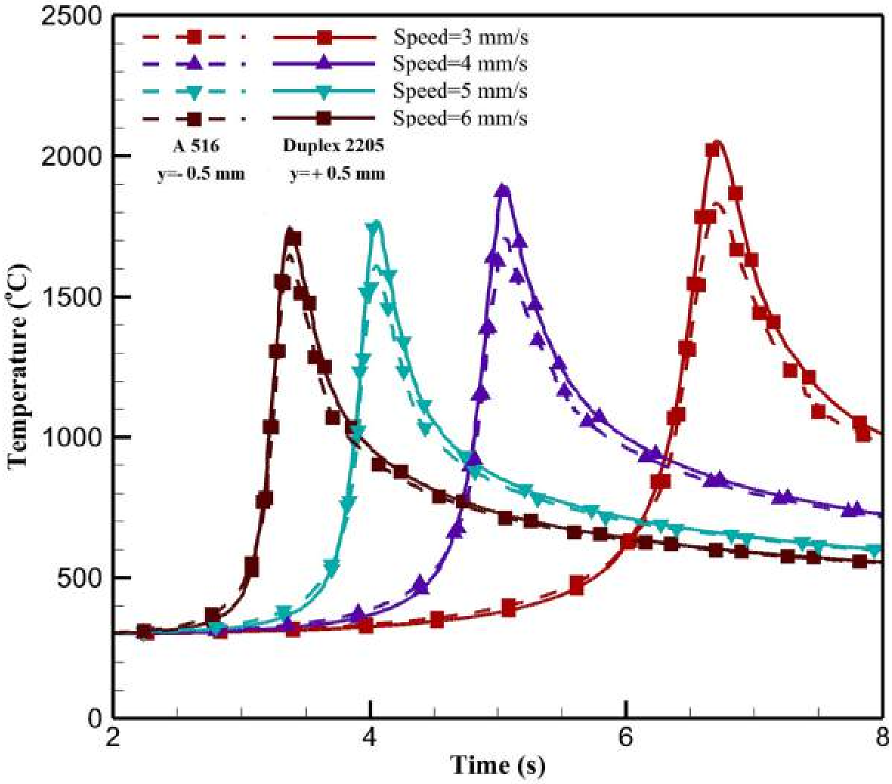

Fig. 11. Temperature history in different welding speed at a power of 400 W (5 mm from the junction).

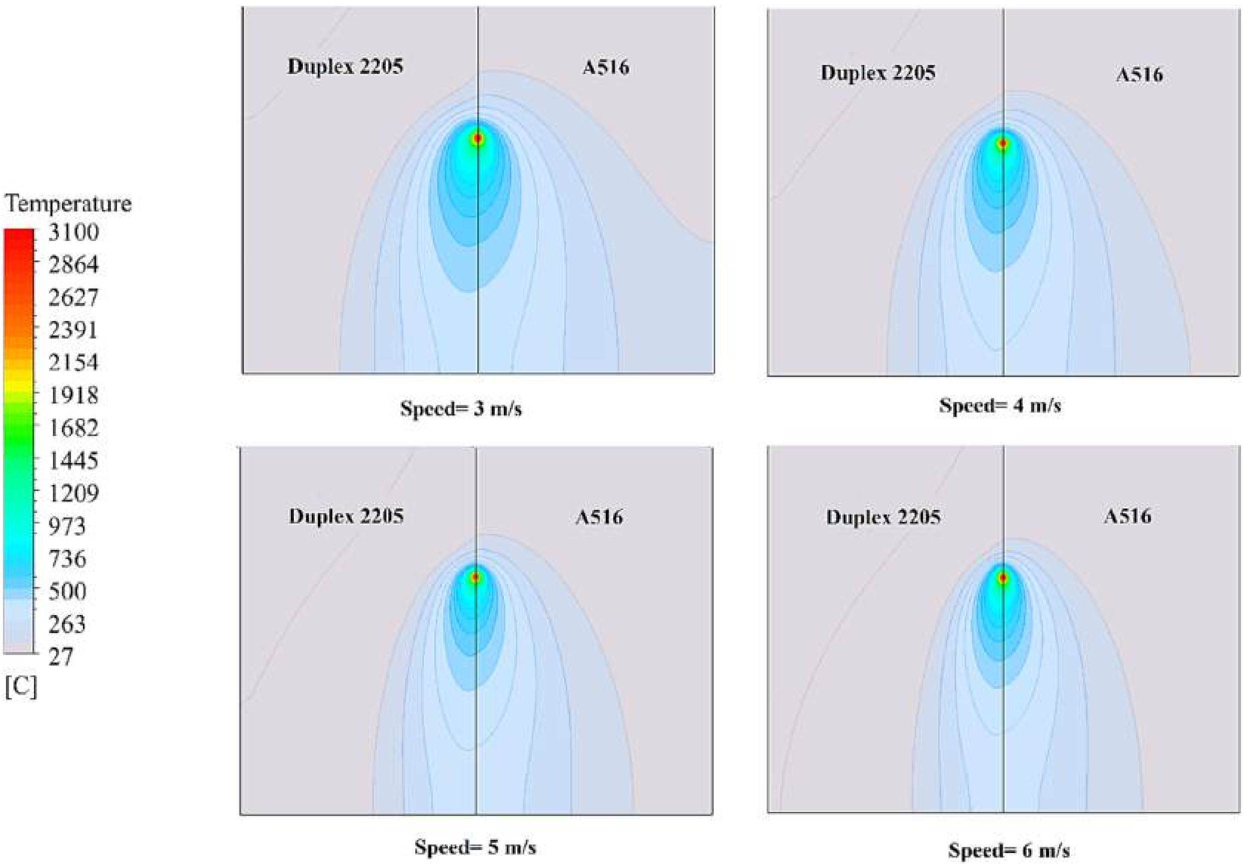

Speed= 3 m/s

Speed= 4 m/s

Speed= 5 m/s

Speed= 6 m/s

Fig. 12. Temperature field on the surface of workpieces at different welding speeds.

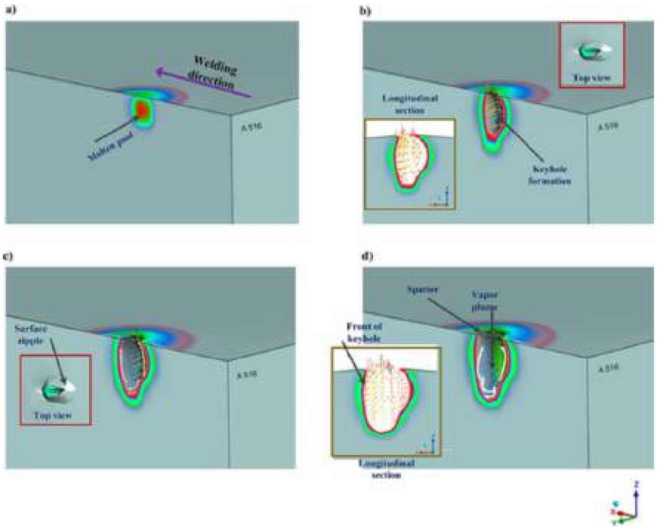

Fig. 13. Dynamic interaction between the molten pool and the keyhole at the interface of two workpieces at power = 450 W and speed = 5 mm/s, a) 24 ms, b) 30 ms, c) 36 ms and d) 42 ms.

4.3. Welding experiments

4.3.1. The effect of laser welding parameters on weld bead characterization

As it is observed in Fig. 15, the variation of weld bead width and shape clearly changed with the increase of laser welding speed in dissimilar laser welding process. Generally, by increasing welding speed from 3 to 5 mm/s, the width of the weld bead reduced about 40 % due to lower laser beam interaction time with the workpiece surface and melted materials. Furthermore, the overlap of weld bead evidently decreased by increasing welding speed and thereby total melt volume decreased. As it was shown in Fig. 11, increasing welding speed reduced the maximum melt pool temperature about 300 °C which in turn decreased the melt volume and thereby the width of the weld bead. As it was observed in Fig. 12, the temperature gradient has been more penetrated toward the duplex stainless steel although the laser beam irradiated the center of the contact line between two workpieces. This phenomenon is clearly observed particularly at lower welding speeds as shown in Fig. 15. The higher thermal conductivity and thereby higher cooling rate of A516 steel reduced the extension of melted material toward it.

In Fig. 16, the effect of increasing laser power on shape and width of the weld bead is observed. It is clearly seen that the width of the weld bead increased about 30 % when the laser beam increased from 400 to 500 W (about 25 % increase rate). It should be noted that after laser power level of 300 W due to having enough melt volume, the weld bead

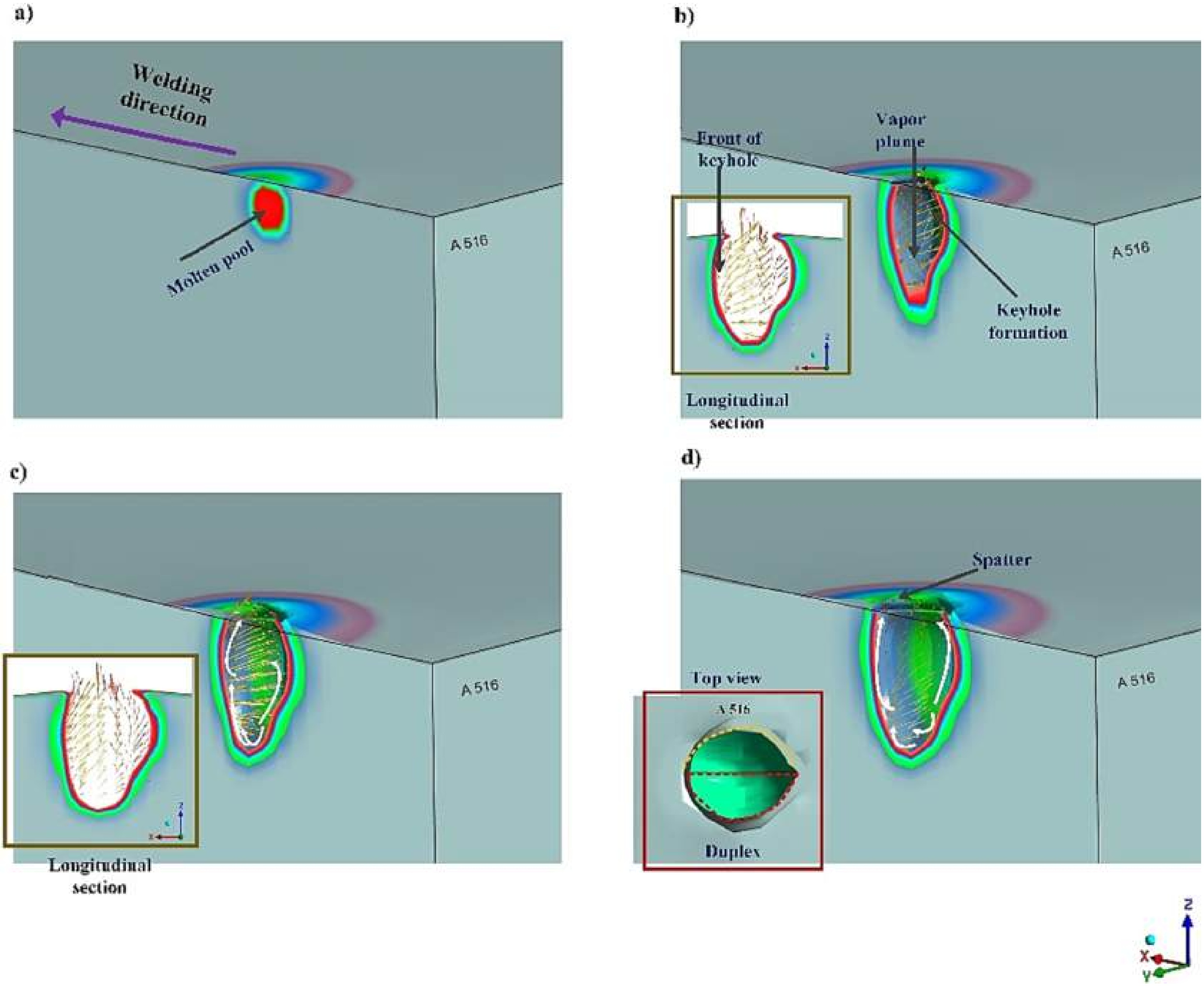

Fig. 14. Dynamic interaction between the molten pool and the keyhole at the interface of two workpieces at power = 500 W and speed = 5 mm/s, a) 24 ms, b) 30 ms, c) 36 ms and d) 46 ms.

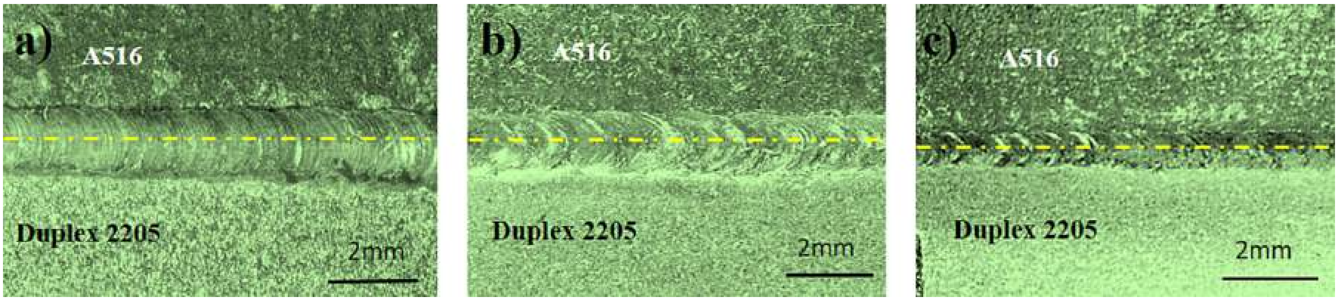

Fig. 15. Weld bead shape at laser power of 400w at focal distance different welding speed of a)3mm/s, b) 4 mm/s, and c) 5 mm/s.

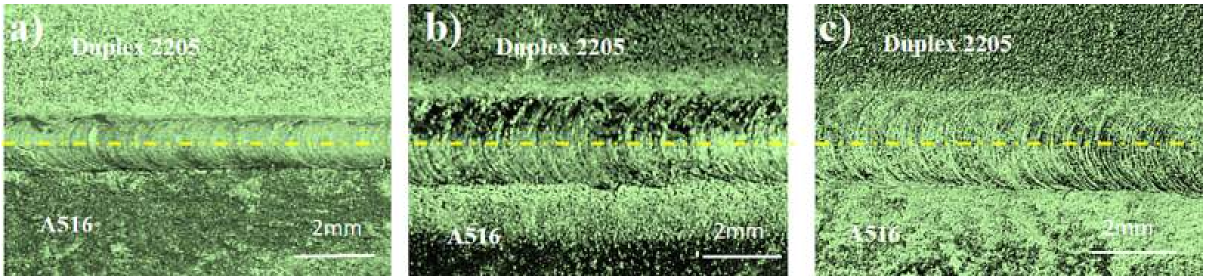

Fig. 16. Weld bead shape at welding speed of 4 mm/s. focal distance 0 mm and different laser power of a) 400 W, b) 450 W, and c) 500 W.

width growth rate changed linearly with the increase of the laser power.

Generally, increasing laser power evidently rises the melt volume and thereby both the width and depth of the melt pool. As it was illustrated in Figs. 8 and 9, the width of the melt pool clearly increased by augmentation of laser power. As shown in Fig. 8, increasing laser power from 400 to 500 W has risen the maximum temperature of melt pool about 900 °C which led to formation of more melt volume and also evaporation of melted materials. On the other hand, Fig. 16 depicts that by increasing laser power, the width of the weld bead remarkably increased and clearly deviated toward duplex stainless steel. Furthermore, as it was mentioned before, it seems the weld bead surface has become more convex when the laser power has increased up to 500 W that is in agreement with partial evaporation of melted material and more possibility of formation of plasma plume during welding. Therefore, it can be concluded that the bulk weld fusion zone composed of duplex stainless steel due to having lower thermal conductivity and accumulation more melted martial toward that by considering lower melting point of duplex stainless steel.

4.3.2. *Microstructural analysis of the dissimilar weld*

Fig. 17 illustrates variation of microstructure of the weld joint form both base metals to the fusion zone according to the temperature gradient induced by laser welding. The A516 steel base metal microstructure is shown Fig. 17b composed of ferrite and pearlite. The HAZ microstructure illustrated in Fig. 17c, transformed from the base metal to the martensitic microstructure. It could be said that the A516 steel heated more than 723 °C at the HAZ region which is followed by rapid cooling to form martensite microstructure due to the higher cooling rate induced by the A516 steel higher thermal conductivity. The fusion zone microstructure composed of combination both metals. Rapid heating more than the melting temperature and thereby fast solidification induced by rapid cooling from base metals created different

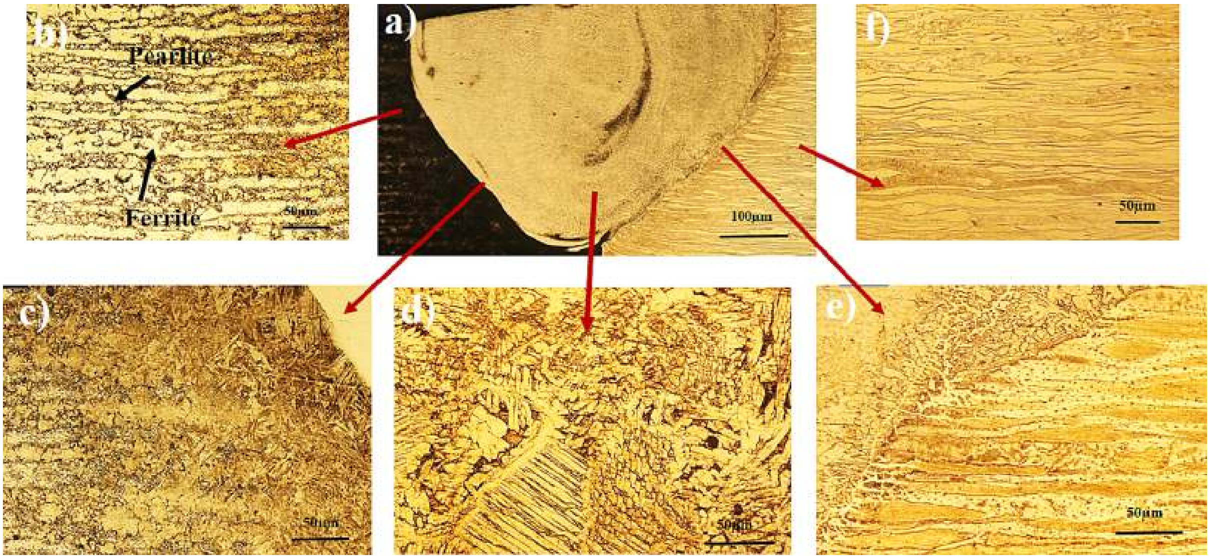

Fig. 17. Microstructure of the dissimilar weld for a) weld joint, b) A516 base metal, c) A516 HAZ, d) Fusion zone, e) Duplex HAZ, and f) Duplex base metal.

microstructural changes. According to the transformation diagram of low carbon steel, the resultant microstructure composed of martensite, acicular ferrite and bainite [47].

The microstructure of duplex stainless steel composed of austenitic grains on ferrite matrix structure. The microstructure of the HAZ region includes due to experiencing heating upper than 800 °C, δ ferrite grains and austenite phases initially formed between ferrite grains. Adjacent to the fusion line of duplex stainless steel because of lower heat input and high cooling rate compared to the fusion zone center the austenitic phase at ferrite grain boundaries formed, as obtained in [48]. The microstructure of the duplex stainless steel at the fusion zone mainly composed of ferritic microstructure, a columnar and cellular dendritic microstructure with coarse-grained austenite on ferrite grain boundary due to fast cooling rate as reported in [48,49].

4.4. Validation

The evaluation of numerical solutions necessitates an examination of the accuracy of the simulation results. In this regard, a comparison was made between the dimensions and configuration of the weld bead in the cross-sectional area of two components, as determined by the numerical and experimental approaches. The congruity was established by employing identical parameters. Fig. 18 presents a comparative analysis of the outcomes achieved at 400 and 450 W power levels and speeds of 4 and 5 mm/s. The graphical representation in Fig. 18 illustrates the favorable precision of the numerical solution in terms of both weld bead shape and dimensions. Consequently, the simulation successfully anticipates the laser welding process.

Based on the observations depicted in Fig. 18, it becomes apparent that an increment of 1 mm/s in welding speed, as compared to Fig. 18b, led to a substantial reduction in the depth and width of the weld bead, resulting in an incorrect connection. The thermal characteristics of duplex stainless steel and A 516 being closely aligned, a nearly equivalent amount of melt formation can be discerned. The outlined lines highlighted on the actual melt pool images shows the area of the fusion zone determined by numerical simulation. The discrepancy particularly observed in Fig. 18.b implies that the lower welding speed can induce more heat dissipation across the weld width and created bigger weld width about 150 μm at upper part of the fusion zone at duplex stainless steel side due to creating higher laser beam interaction time with melted material and thereby accumulation of the melted material at this region.

5. Conclusions

This research focused on the empirical and computational examination of laser fusion welding between two dissimilar alloys of A516 and duplex stainless steel. A numerical model was developed by using a combined heat source to simulate the intricate dynamics associated with the keyhole properties by considering both different melt flow of dissimilar metals and the effect of the recoil pressure of vaporized metal through generating distortion of the interface between the liquid and vapor phases.

- This study presented a prediction model and experimental validation of dissimilar weld bead geometry through both the weld bead top surface and weld bead depth simultaneously via prediction of combined model of temperature field, melt flow and evaporation of metals. Therefore, the effect of metals evaporation on melt flow has additionally considered apart from the effect of temperature gradient.
- The temperature distribution from simulation results has a good correlation with the microstructural changes of the dissimilar melt pool region according to the higher melting efficiency of duplex stainless steel as means of the main part of the melted material and higher solidification rate of duplex stainless steel induced by higher thermal conductivity of A516 steel by creation steeper cooling rate at the dissimilar melt pool region and steep adjacent HAZ of A516 base metal.
- The temporal variations of temperature for increasing laser power from 350 to 500 W at a speed of 5 mm/s, illustrated a nonlinear relationship of temperature increment. Notably, the temperature at its peak experiences a surge up to 3800oC upon the rising the power from 450 to 500 W. In accordance with the graphical representation, discernible is the inverse correlation between the augmentation of

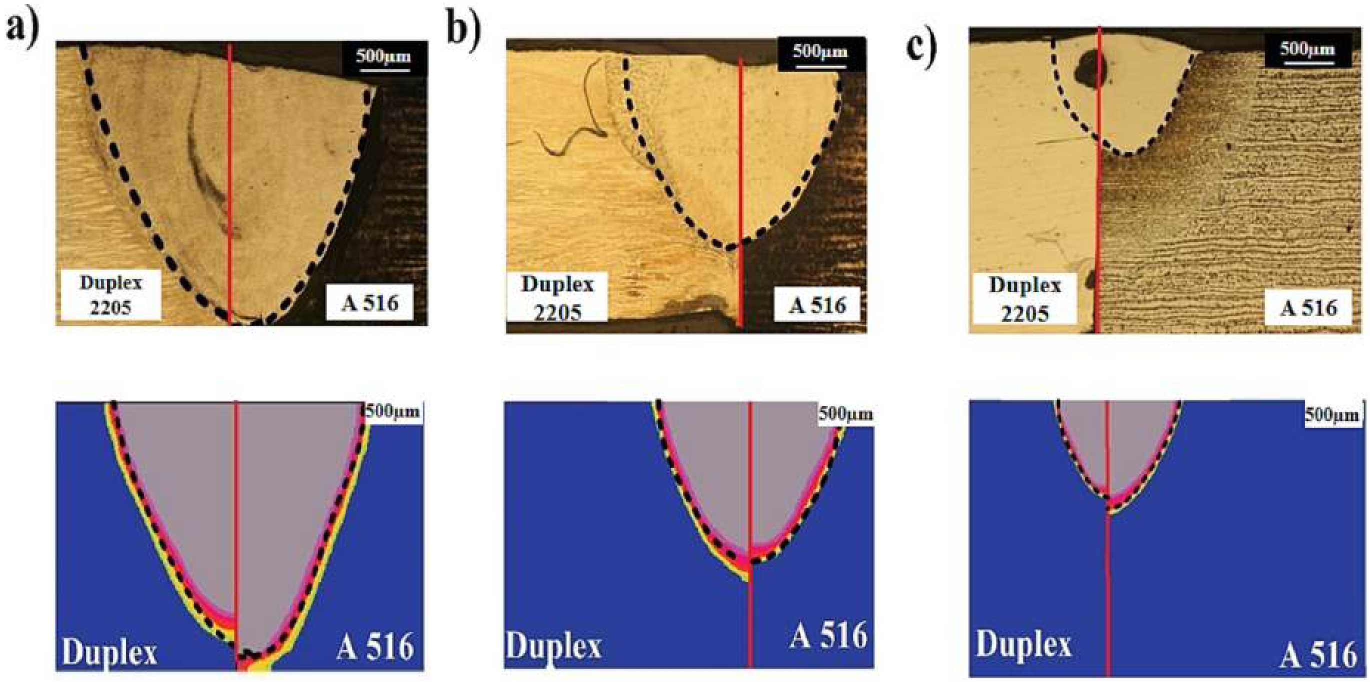

Fig. 18. Weld profile comparison between simulation and experiment results a) power = 450 W, speed = 5 mm/s, b) power = 400 W, speed = 4 mm/s, and c) power = 400 W, speed = 5 mm/s.

laser power and the reduction in the duration required to attain the zenith temperature.

- The time history of temperature at different welding speeds, especially at a distance of 5 mm from the joint, showed that the duplex stainless steel component has had higher temperatures compared to the A516 material at certain time intervals due to lower heat conduction and higher melting volume compared to A516 steel.
- The constant temperature lines become oval as a result of the increased speed, and the quantity of heat penetration to the surrounding regions diminishes significantly as the welding speed rises due to the shortening of the laser beam's energy absorption period.
- A local bump on the surface was formed due to intense evaporation and expansion caused by the temperature gradient. Also, the vapor generated in the keyhole tends to move near the wall due to the temperature gradient.
- The model presented the interaction between solid region, the molten pool, and the metal vapor. At laser power of 500 W and welding speed of 5 mm/s, the keyhole was formed due to heightened energy absorption, that the extreme temperature gradient and also the vapor movement within the keyhole near the wall. the highest velocity created because of enhanced thermal penetration rate.
- The melt pool geometry predicted from the simulation results (melt flow and temperature field) has been in good agreement with the melt pool geometry extracted by the experiment.
- The temperature distribution from simulation results has a good correlation with the microstructural changes of the melt pool region according to the melting, solidification and temperature gradient at the melt pool region and adjacent HAZ of base metals.

CRediT authorship contribution statement

Yuelei Zhang: Visualization, Writing – review & editing. **Mohammad Hossein Razavi Dehkordi:** Project administration, Supervision. **Mohammad Javad Kholoud:** Project administration, Supervision. **Hamidreza Azimy:** Conceptualization, Investigation, Writing – original draft. **Z. Li:** Supervision, Writing – review & editing. **Mohammad Akbari:** Project administration, Supervision.

Declaration of competing interest

The authors declare that they have no known competing financial interests or personal relationships that could have appeared to influence the work reported in this paper.

Data availability

The authors do not have permission to share data.

Acknowledgements

This research was supported by the Science Foundation of Donghai Laboratory (No. DH-2022KF0302) and the Opole University of Technology as part of the GRAS project no. 270/23.

References

[1] P. Preethi, H.R. Mamatha, Region-based convolutional neural network for segmenting text in epigraphical images, Artificial Intelligence and Applicatons 1 (2) (2021) 119–127, https://doi.org/10.47852/bonviewAIA2202293.

[2] B. Fan, et al., Intelligent vehicle lateral control based on radial basis function neural network, sliding mode controller, CAAI Trans. Intell. Technol. 7 (3) (2022) 455–468, https://doi.org/10.1049/cit2.12075.

[3] H. Taherdoost, M. Madanchian, Analytic Network Process (ANP) method: A comprehensive review of applications, advantages, and limitations, Journal of Data Science and Intelligent Systems (2023), https://doi.org/10.47852/bonviewJDSIS3202885.

[4] S. Saminu, et al., Applications of artificial intelligence in automatic detection of epileptic seizures using EEG signals: A review, Artificial Intelligence and Applications 1 (1) (2023) 11–25, https://doi.org/10.47852/bonviewAIA2202297.

[5] M. Asmael, A. Memarzadeh, A review on recent achievements and challenges in. electrochemical machining of tungsten carbide. Archives of Advanced Engineering, Science. (2023), https://doi.org/10.47852/bonviewAAES3202915.

[6] Erum, N., Ahmad J.: Structural, elastic and mechanical properties of cubic perovskite. materials. Archives of Advanced Engineering Science. (2023). Doi: 10.47852./bonviewAAES3202944.

[7] O. Shekoofa, J. Wang, D. Li, Fabrication of n-type nanocrystalline silicon thin-film by. magnetron sputtering and antimony induced crystallization. Archives of Advanced. Engineering, Science. (2023), https://doi.org/10.47852/bonviewAAES32021040.

[8] A. Karimi, A. Karimipour, M. Akbari, M. Mehdi Razzaghi, G.M. Jamali, Investigating the mechanical properties and fusion zone microstructure of dissimilar laser weld joint of duplex 2205 stainless steel and A516 carbon steel, Optics & Laser Technology. 158 (2023) 108875.

[9] M. Azari, E. Rasti, M.H.R. Dehkordi, H. Azimy, A. Zarei, S.A. Bagherzadeh, Investigation of temperature distribution and melt pool microstructure in laser fusion welding of Inconel 625 superalloy, Journal of Laser Applications. 33 (2) (2021) 022015.

[10] Y. Geng, M. Akbari, A. Karimipour, A. Karimi, A. Soleimani, M. Afrand, Effects of the laser parameters on the mechanical properties and microstructure of weld joint in dissimilar pulsed laser welding of AISI 304 and AISI 420, Infrared Physics & Technology 103 (2019) 103081.

[11] Z. Li, K. Rostam, A. Panjehpour, M. Akbari, A. Karimipour, S. Rostami, Experimental and numerical study of temperature field and molten pool dimensions in dissimilar thickness laser welding of Ti6Al4V alloy, Journal of Manufacturing Processes. 49 (2020) 438–446.

[12] J. Wang, Z. Sun, L. Gu, H. Azimy, Investigating the effect of laser cutting parameters on the cut quality of Inconel 625 using Response Surface Method (RSM), Infrared Physics & Technology. 118 (2021) 103866.

[13] Y. Yongbin, S.A. Bagherzadeh, H. Azimy, M. Akbari, A. Karimipour, Comparison of the artificial neural network model prediction and the experimental results for cutting region temperature and surface roughness in laser cutting of AL6061T6 alloy, Infrared Physics & Technology. 108 (2020) 103364.

[14] S.H. Jung, H.J. Kim, Application of laser welding to STS301L side structure of railway vehicles (||) - incidence angle welding conditions for laser beam based on multiple regression analysis of dummy variables, Journal of Mechanical Science and Technology (2023).

[15] C. Sun, M.H.R. Dehkordi, M.J. Kholoud, H. Azimy, Z. Li, Systematic evaluation of pulsed laser parameters effect on temperature distribution in dissimilar laser welding: A numerical simulation and artificial neural network, Optics & Laser Technology. 163 (2023) 109407.

[16] A.I. Khdair, A.B. Khoshaim, K.A. Alnefaie, Evaluation of the effect of filler metal interlayer on the weld joint quality in fiber laser welding of alloy steel (A516), Journal of Laser Applications. 34 (1) (2021) 012011.

[17] Q. Nguyen, S.A. Bagherzadeh, A. Parsian, M. Akbari, A. Karimipour, A. Mosavi, Nonlinear model identification of dissimilar laser joining of S.S 304 and ABS using the Hammerstein-Wiener method, Optik. 225 (2021) 165649.

[18] Q. Nguyen, A. Azadkhou, M. Akbari, A. Panjehpour, A. Karimipour, Experimental investigation of temperature field and fusion zone microstructure in dissimilar pulsed laser welding of austenitic stainless steel and copper, Journal of Manufacturing Processes. 56 (2020) 206–215.

[19] A. Baghdadchi, V.A. Hosseini, K. Hurtig, L. Karlsson, Promoting austenite formation in laser welding of duplex stainless steel—impact of shielding gas and laser reheating, Welding in the World. 65 (3) (2021) 499–511.

[20] A. Mosavi, A. Soleimani, A. Karimi, M. Akbari, A. Karimipour, A. Karimipour, Investigating the effect of process parameters on the mechanical properties and temperature distribution in fiber laser welding of AISI304 and AISI 420 sheet using response surface methodology, Infrared Physics & Technology. 111 (2020) 103478.

[21] M. Landowski, A. Świerczyńska, G. Rogalski, D. Fydrych, Autogenous Fiber Laser Welding of 316L Austenitic and 2304 Lean Duplex Stainless Steels, Materials [internet]. 13 (13) (2020).

[22] S. Saravanan, K. Raghukandan, N. Sivagurumanikandan, Pulsed Nd: YAG laser welding and subsequent post-weld heat treatment on super duplex stainless steel, Journal of Manufacturing Processes. 25 (2017) 284–289.

[23] R. Lai, Y. Cai, Y. Wu, F. Li, X. Hua, Influence of absorbed nitrogen on microstructure and corrosion resistance of 2205 duplex stainless steel joint processed by fiber laser welding, Journal of Materials Processing Technology. 231 (2016) 397–405.

[24] Chen J, Laver A, Zavadil R, Liang J, Zheng W, editors. Laser and electron beam welding of 25 mm thick A516 Gr. 70 steel. International Congress on Applications of Lasers & Electro-Optics; 2013: Laser Institute of America.

[25] P. Sahoo, T. Debroy, M. McNallan, Surface tension of binary metal—surface active solute systems under conditions relevant to welding metallurgy, Metallurgical Transactions b. 19 (1988) 483–491.

[26] Y. Ai, P. Jiang, X. Shao, P. Li, C. Wang, A three-dimensional numerical simulation model for weld characteristics analysis in fiber laser keyhole welding, International Journal of Heat and Mass Transfer. 108 (2017) 614–626.

[27] W. Ke, X. Bu, J. Oliveira, W. Xu, Z. Wang, Z. Zeng, Modeling and numerical study of keyhole-induced porosity formation in laser beam oscillating welding of 5A06 aluminum alloy, Optics & Laser Technology. 133 (2021) 106540.

[28] S. Katayama, Handbook of laser welding technologies, Elsevier (2013).

[29] P. Coppa, A. Consorti, Normal emissivity of samples surrounded by surfaces at diverse temperatures, Measurement. 38 (2) (2005) 124–131.

[30] M.J. Kholoud, M. Akbari, Numerical investigation of molten pool dimension, temperature field and melting flow during pulsed laser welding of Ti-6Al-4V alloy sheets with different thicknesses, Journal of Laser Applications. 33 (3) (2021).

[31] I. Tlili, D. Baleanu, S. Mohammad Sajadi, F. Ghaemi, M.A. Fagiry, Numerical and experimental analysis of temperature distribution and melt flow in fiber laser welding of Inconel 625, The International Journal of Advanced Manufacturing Technology. 121 (1–2) (2022) 765–784.

[32] Y. Ai, X. Liu, Y. Huang, L. Yu, Investigation of dissimilar fiber laser welding of low carbon steel and stainless steel by numerical simulation, Journal of Laser Applications. 33 (1) (2021).

[33] Y. Ai, P. Jiang, C. Wang, G. Mi, S. Geng, W. Liu, et al., Investigation of the humping formation in the high power and high speed laser welding, Optics and Lasers in Engineering. 107 (2018) 102–111.

[34] Y. Ai, P. Jiang, C. Wang, G. Mi, S. Geng, Experimental and numerical analysis of molten pool and keyhole profile during high-power deep-penetration laser welding, International Journal of Heat and Mass Transfer. 126 (2018) 779–789.

[35] Y. Ai, X. Shao, P. Jiang, P. Li, Y. Liu, W. Liu, Welded joints integrity analysis and optimization for fiber laser welding of dissimilar materials, Optics and Lasers in Engineering. 86 (2016) 62–74.

[36] Y. Ai, L. Yu, Y. Huang, X. Liu, The investigation of molten pool dynamic behaviors during the "∞" shaped oscillating laser welding of aluminum alloy, International Journal of Thermal Sciences. 173 (2022) 107350.

[37] B. Chang, C. Allen, J. Blackburn, P. Hilton, D. Du, Fluid flow characteristics and porosity behavior in full penetration laser welding of a titanium alloy, Metallurgical and Materials Transactions b. 46 (2015) 906–918.

[38] J.G. Berryman, S.C. Blair, Kozeny-Carman relations and image processing methods for estimating Darcy's constant, Journal of Applied Physics. 62 (6) (1987) 2221–2228.

[39] S. Pang, K. Hirano, R. Fabbro, T. Jiang, Explanation of penetration depth variation during laser welding under variable ambient pressure, Journal of Laser Applications. 27 (2) (2015).

[40] B. Hu, S. Hu, J. Shen, Y. Li, Modeling of keyhole dynamics and analysis of energy absorption efficiency based on Fresnel law during deep-penetration laser spot welding, Computational Materials Science. 97 (2015) 48–54.

[41] M. Daha, G. Nassef, I. Abdallah, H. AbouSeeda, Three-dimensional thermal finite element modeling for keyhole plasma arc welding of 2205 duplex stainless steel plates, International Journal of Engineering and Technology. 2 (4) (2012) 720–728.

[42] A. Shahzad, Thermophysical Properties of Complex Materials, BoD–Books on Demand (2020).

[43] K. Thurnay, Thermal properties of transition metals, Forschungszentrum Karlsruhe Karlsruhe (1998).

[44] G. Grimvall, Thermophysical properties of materials, Elsevier (1999).

[45] A. Ghosh, D. Misra, S. Acharyya, Numerical simulation of the laser welding of 2205 duplex stainless steel, Int J Laser Sci. 1 (2019) 293–313.

[46] K.C. Mills, Recommended values of thermophysical properties for selected commercial alloys, Woodhead Publishing, 2002.

[47] C.R. Brooks, Principles of the heat treatment of plain carbon and low alloy steels, ASM International (1996).

[48] C. Köse, Dissimilar laser beam welding of AISI 420 martensitic stainless steel to AISI 2205 duplex stainless steel: effect of post-weld heat treatment on microstructure and mechanical properties, Journal of Materials Engineering and Performance. 30 (10) (2021) 7417–7448.

[49] V. Hosseini, Influence of multiple welding cycles on microstructure and corrosion resistance of a super duplex stainless steel, University West, 2016.